Applied Catalysis B: Environmental 219 (2017) 391–400

Contents lists available at ScienceDirect

Applied Catalysis B: Environmental

journal homepage: www.elsevier.com/locate/apcatb

Titania nanosheet photocatalysts with dominantly exposed (001) reactive facets for photocatalytic NOx abatement

Joseph Che-Chin Yu[a], Van-Huy Nguyen[b], Janusz Lasek[c], Jeffrey C.S. Wu[a,*]

[a] Department of Chemical Engineering, National Taiwan University, Taipei 10617, Taiwan
[b] Faculty of Chemical and Environmental Engineering, Lac Hong University, No. 10 Huynh Van Nghe, Buu Long, Bien Hoa, Dong Nai, Viet Nam
[c] Institute for Chemical Processing of Coal, ul. Zamkowa 1, 41-803 Zabrze, Poland

ARTICLE INFO

Article history:
Received 14 May 2017
Received in revised form 23 July 2017
Accepted 26 July 2017
Available online 27 July 2017

Keywords:
TiO_2 nanosheet
(001) Reactive facet
NOx abatement
Photocatalyst
Reaction pathway

ABSTRACT

The particular role of reactive facets TiO_2 on photocatalytic NOx removal was systematically explored. The photo selective catalytic reduction (photo-SCR) of NOx was studied using titania nanosheet photocatalysts. The titania nanosheets were synthesized by hydrothermal method with titanium *n*-butoxide (TBOT) and hydrofluoric acid (HF). The synthetic pathway of transformation from TBOT (Ti precursor) to TiO_2 nanosheet was clearly revealed that $TiOF_2$ is the intermediate during the hydrothermal process. The NO conversion of titania nanosheets was found to be higher than the conversion of commercial P25 and TiO_2 synthesized by the sol-gel method. Moreover, one of the titania nanosheets, FT1.5, displayed the highest efficiency of NOx removal at 393 K, but there was a trade-off relationship between NO conversion and NO_2 selectivity. Our results suggest that the optimal synthetic process for highest efficiency of TiO_2 nanosheet in photocatalysis is to use TBOT and HF with the F/Ti atomic ratio = 1.5 (FT1.5) at 453 K for 24 h. In summary, the synthesized TiO_2 nanosheet exhibits great potential to be applied in NOx abatement.

1. Introduction

Nitrogen oxide ($NO_{(g)}$) is one of the main components in flue gas emitted from stationary sources during the combustion processes. It is recognized as one of the tropospheric air pollutants, and it would be easily oxidized by ozone or radicals to generate nitrogen dioxides ($NO_{2(g)}$) in the atmosphere [1,2]. Since NO_2 has been proved to bring about respiratory system problems such as asthma [3], or even lead to pneumonia or lung cancer [4] of human beings, it has been listed as one of the criteria pollutants as shown in Table 1. Furthermore, NO_2 can participate in the complicated photochemical reaction, forming ozone (O_3) under the sunlight irradiation [5]. It was also reported that NOx ($NO + NO_2$) has a strong correlation with the formation of atmospheric particulate matter (PM) that have a diameter less than 2.5 micrometers ($PM_{2.5}$) [6]. Note that both O_3 and PM also belong to criteria pollutants as listed in Table 1, due to their confirmed health effects on mankind [7,8]. It clearly shows that among six kinds of criteria pollutants, half of them can be directly or indirectly generated from NOx. Thus, research in the field of NOx abatement has grown significantly recently.

Among de-NOx technologies, photo-assisted selective catalytic reduction (photo-SCR) is an advanced technology which can be operated at a relatively low temperature in comparison with the traditional selective catalytic reduction (SCR) which requires a high temperature. So far the main concern of photo-SCR has been its low GHSV (gas hour space velocity) that made it difficulty applied in the industry [9]. Accordingly, the GHSV was set at 10000 h^{-1} in this study to meet the requirement of stationary emission sources [10]. In general, there are three kinds of reductants in the photo-SCR process, including ammonia (denoted as NH_3-photo-SCR) [11], hydrocarbons (HC-photo-SCR) [12], and carbon monoxide (CO-photo-SCR) [13]. In this work, the HC-photo-SCR was deliberately chosen to simulate the conditions in the industry, such as power plants, where the remained hydrocarbons exist in the flue gas emitted through the combustion processes [14].

Anatase TiO_2 with a high percentage of reactive (001) facets, so-called titania nanosheet due to its shape, was reported in 2008 [15]. The (001) surface with a surface energy of 0.98 J m^{-2}, which has been demonstrated to have a higher reactivity than (101) surface of 0.49 J m^{-2} or (100) surface of 0.58 J m^{-2} [16,17]. Titania nanosheet and its derived materials have been applied in diverse categories of photocatalysis with outstanding performance, including organics degradation [18,19], H_2 production [20,21], CO_2 reduction [2,22]. Although the (001) surface has a very high surface energy, maximizing the percentage of exposed (001) area might not be a good direction. There exists an optimal ratio of the exposed (001) and (101) facets under certain conditions [2]. Based on the calculation results of density functional theory (DFT), a suitable ratio of the

* Corresponding author.
E-mail address: cswu@ntu.edu.tw (J.C.S. Wu).

http://dx.doi.org/10.1016/j.apcatb.2017.07.077
0926-3373/

Table 1
National Ambient Air Quality Standards (NAAQS, the table was reproduced according to latest announcement of EPA).

Pollutant		Primary/Secondary	Averaging Time	Level
Carbon Monoxide (CO)	primary	8 h	9 ppm	
	1 h		35 ppm	
Lead (Pb)		primary and secondary	Rolling 3 month average	0.15 μg/m^3
Nitrogen Dioxide (NO_2)	primary	1 h	100 ppb	
	primary and secondary	1 year	53 ppb	
Ozone (O_3)		primary and secondary	8 h	0.070 ppm
Particle Pollution (PM)	$PM_{2.5}$	primary	1 year	12.0 μg/m^3
		secondary	1 year	15.0 μg/m^3
	PM_{10}	primary and secondary	24 h	35 μg/m^3
		primary and secondary	24 h	150 μg/m^3
Sulfur Dioxide (SO_2)	primary	1 h	75 ppb	
	secondary	3 h	0.5 ppm	

exposed (001) and (101) facets could avoid the electrons and holes accumulate on the (101) facets or overflow to the (001) facets. The optimal ratio of exposed (001) and (001) facets can improve the migration of electrons and holes between (101) and (001) facets so that photocatalytic activity is enhanced [2]. Therefore, this study intends to find an optimal synthetic recipe for titania nanosheet to efficiently remove NOx.

Among the typical synthetic methods, titanium(IV) butoxide (TBOT) and hydrofluoric acid (HF) are the most common precursors to provide Ti^{4+} and F^- ion [23]. After the hydrothermal treatment, the anatase titania nanosheets can be well synthesized. In the reported X-ray diffraction characterizations, besides the main (101) anatase peak of samples, another subtle peak at $2\theta = 23.9^\circ$, which is referred to as a $TiOF_2$ compound in the JCPDS database no. 08-0060, can be observed. Yet people seldom discussed this subtle peak in detail. Thus, in the present work, we explored the best synthetic conditions, including the ratio of precursors, temperature, and duration of the hydrothermal process. This method for synthesis of titania nanosheets is universally suitable for different photocatalytic reactions. Finally, the formation pathway of titania nanosheets is proposed based on our own experience and literatures. How the exposed (001) facets of titania nanosheet affects the photocatalytic activity in NOx removal, including catalytic performance and reaction mechanism, was also conducted from the point of view of redox abilities of photocatalysts. To the best of our knowledge, for the first time, the particular role of reactive facets on photocatalytic NOx removal has been systematically studied.

2. Experimental

2.1. Preparation of photocatalysts

There were five TiO_2 photocatalysts tested in this study, P25, SG, FT1, FT1.5 and FT2 (these labels were explained as followed). The first one is the commercial P25 TiO_2 photocatalyst (Evonik Degussa, Aeroxide® P25, >99.5%), a well-known TiO_2 photocatalyst used as a standard to compare with the other photocatalysts. It would be named as "P25" hereafter. Next, the TiO_2 photocatalyst prepared by the sol-gel method is called "SG". The synthetic procedure was referred to our previous study [24]. The 17.50 g of precursor titanium (IV) butoxide (TBOT, Alfa Aesar, 99+%) was added into 100.0 ml of 0.10 M HNO_3 (J.T. Baker®, 65%) drop by drop at 298 K. Afterward, the solution was vigorously stirred at the rate of 600 rpm and heated to 353 K for 8 h to complete the hydrolysis process. The as-prepared sol-gel would be calcined at 773 K for 3 h to form the crystalline phases. Lastly, the powder was ground with an agate mortar and then the particulate TiO_2 could be obtained. Since this SG sample has been investigated by our previous study [24], it is a candidate of "particulate" TiO_2 to compare with the "sheet-like" TiO_2 as followed.

The titania nanosheets were prepared by the hydrothermal method according to typical procedures from literatures with a slight modification [18,20,25]. At first, 50.0 g of Titanium (IV) *n*-butoxide (TBOT, Alfa Aesar, 99+%) was mixed with different amounts of hydrofluoric acid (HF, Sigma-Aldrich, 48%), 6.124, 9.186 and 12.248 g. These amounts of HF were intendedly calculated based on the nominal F/Ti atomic molar ratio which equaled to 1, 1.5, and 2. Therefore, they were named as "FT1", "FT1.5", and "FT2", respectively. After vigorously stirring in 100 ml Teflon-lined stainless steel autoclave for 30 min at 298 K, the mixed solution was placed in an oven at 453 K for 24 h. The autoclave was then cooled down for 8 h at 298 K after the hydrothermal reaction. Each sample was washed with deionized water and ethanol three times, followed by a drying process at 353 K for additional 8 h. Finally, the titania nanosheets, FT1, FT1.5, and FT2, were obtained after grinding.

2.2. Characterization of photocatalysts

A powder X-ray diffractometer (XRD, Rigaku) with Cu-Kα radiation ($\lambda = 1.5418$ Å) at a scanning rate of 10° (2θ) min^{-1} was used to confirm the crystalline structure and determine the crystalline size of the photocatalysts. The crystalline size was calculated according to the modified Scherrer equation that took every peak in an XRD spectrum into account. This modified Scherrer equation was proposed to decrease the systematic error of Scherrer equation [26]. The surface morphology of the photocatalysts was observed by a scanning electron microscopy (SEM, Nova NanoSEM 230) and a transmission electron microscopy (TEM, JEOL™ JEM-1200EX II). A high-resolution transmission electron microscopy (HRTEM, Phillips Tecnai F20 G2 FEI-TEM) equipped with an energy dispersive X-ray spectroscopy (EDS) detector was used to explore the selected area diffraction (SAED) pattern and d-spacing of the titania nanosheets. To estimate the particle sizes, a considerable amount of well-defined titania nanosheets was counted one by one. For the precise edge lengths of titania nanosheets, both the width and length of each rectangular would be measured. The difference between width and length should be less than 10% to prevent from the misjudgments. Brunauer-Emmett-Teller (BET) analysis using a nitrogen adsorption apparatus (ASAP 2010, Micromeritics) was conducted to acquire the specific surface area of the photocatalysts. All samples were degassed at 110 °C overnight before the multipoint measurements. A UV–vis spectrometer (Varian Cary 100) equipped with an integrating sphere was used to obtain the diffuse reflectance UV–vis spectra of the photocatalysts. The optical absorption range was measured in 200–800 nm. An X-ray photoelectron spectroscopy (XPS, Thermal Fisher Scientific Theta Probe) equipped with Al-Kα X-ray source (1486.6 eV) was performed to investigate the chemical status of elements. All of the samples were pretreated with the same conditions. The powder samples were tableted, and then their surfaces were cleaned by Ar-gas cluster

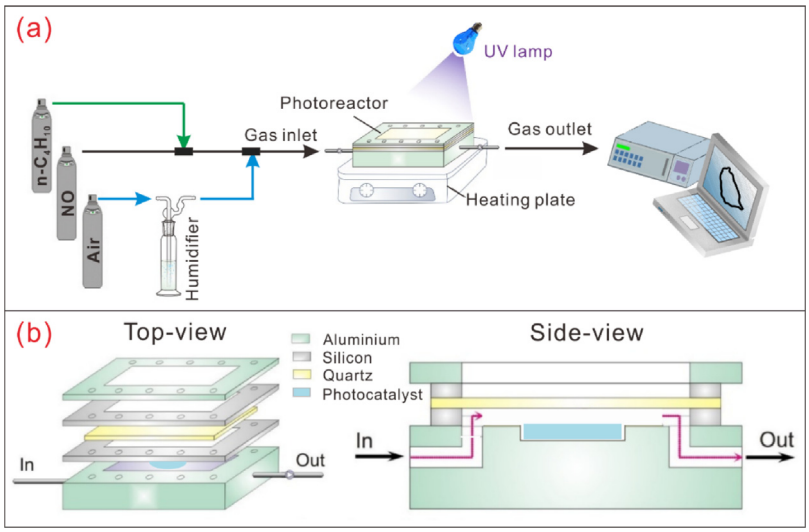

Fig. 1. (a) Schematic design of experimental apparatus for photo-SCR. (b) Illustration of top-view and side view of plate-shape photoreactor engraved with a cylindrical notch.

ion source. For peaks deconvolution of Ti element in XPS spectra, the following parameters were applied based on the reference [27], that is, pass energy = 20 eV, FWHM = 1.02 and 1.98 eV for Ti^{4+} $2p_{3/2}$ and Ti^{4+} $2p_{1/2}$, respectively; the splitting between Ti^{4+} $2p_{3/2}$ and Ti^{4+} $2p_{1/2}$ = 5.72 eV for the dominant anatase phase of titania nanosheets; Gaussian (33%)-Lorentzian (67%) for Ti element; the area below the Ti^{4+} $2p_{1/2}$ curve being half of the area below the Ti^{4+} $2p_{3/2}$ curve. Dynamic light scattering (DLS, Malvern™ Zetasizer Nano ZS) was used to measure the particle size and particle size distribution of the photocatalysts. Photoluminescence (PL) spectra for titania nanosheets were conducted by fluorescence spectrophotometer equipped with 150 W xenon lamp (HITACHI, F-7000) to check the recombination rates of photo-generated holes and electrons.

2.3. Apparatus

The apparatus of photo-SCR experiments is shown in Fig. 1, and it was slightly modified according to our previous study [28]. The photocatalysts of 0.0300 g were placed on central position engraved with a cylindrical notch with 15 mm in diameter and 1 mm in height. This design is to ensure the photocatalysts evenly disperse on the photoreactor so that the exposure area of UV light irradiation can be kept as a constant, 176.63 mm^2. The feeding composition of all photo-SCR experiments was 400 ppmv NO, 2000 ppmv C_4H_{10}, 4 v% H_2O, 4 v% O_2, and N_2 balance. The volume flow rate of feeding gas was controlled at $25.0 \pm 2\%$ ml min^{-1}, which corresponds to gas hour space velocity (GHSV) of 10000 h^{-1}. Note that the NO concentration was chosen at 400 ppmv because it is seldom higher than this value in either flue gases or exhaust gases since the control of combustion processes and the emission control of NO have been improved year by year [29]. A mercury arc lamp equipped with a filter of 320–500 nm wavelength (EXFO Omnicure S1500, 200 mW cm^{-2}) was used in the experiments. The concentration of NO, NO_2, NOx was immediately monitored and recorded by an online chemiluminescence nitrogen oxides analyzer (Teledyne, Model 200E) every minute. The NO conversion, NO_2 selectivity, and NOx removal were calculated based on the molar basis as following Eqs. (1)–(3):

$$\text{NO conversion} = \left(\frac{NO_{inlet} - NO_{outlet}}{NO_{inlet}}\right) \times 100\% \quad (1)$$

$$NO_2 \text{ selectivity} = \left(\frac{NO_2 \text{ outlet} - NO_2 \text{ inlet} NO_{inlet} - NO_{outlet}}{}\right) \times 100\% \quad (2)$$

$$NO_x \text{ removal} = \left(\frac{NO_x \text{ inlet} - NO_x \text{ outlet} NO_x \text{ inlet}}{}\right) \times 100\% \quad (3)$$

All experiments were carried out in the same procedure. The total recorded time was 240 min for each experiment, including three intervals: (1) The initial 30-min purge to ensure the NO concentration was stable. (2) After the initial 30 min, the UV light was turned on and the photo-SCR started. The photo-SCR was conducted for 180 min and then the UV light was turned off. (3) The NO was kept monitoring in the last 30 min to confirm the NO concentration remained the same as the initial value. The photocatalyst was replaced as a fresh one after each 240-min test. The photo-SCR was carried out at four conditions of reaction temperature, 313, 353, 393 and 433 K, respectively. For titania nanosheets (FT1, FT1.5, and FT2), each photocatalyst was performed three times at different temperatures. For comparison, P25 and SG photocatalysts, which were reported in previous studies, were carried out one time at different temperatures [24,30]. Considering to acquire accurate activities of photocatalysts, in the data processing, all values of outlet concentration (NO_{outlet}, $NO_{2outlet}$, and NOx_{outlet}) were the average of the last five minutes before the UV light was turned off.

3. Results and discussion

3.1. Characterization of photocatalysts

Fig. 2 shows the diffuse reflectance UV–vis spectra of different photocatalysts. All of the samples except SG had the main absorption edge below 400 nm where is the absorption range of UV light. This result was also consistent with the observed color of these samples. SG exhibited a slightly yellowish color, whereas the other samples exhibited a white color. The slightly yellowish color of SG can be explained by the doping effect of nitrogen atoms. The doped nitrogen atoms can narrow the band gap by increasing the potential of valance band. The lower value of band gap leads to the red shift in UV–vis spectra. It was reported that the light absorption can be shifted to the visible light region when nitrogen atoms are introduced into TiO_2 lattice [31–33]. In the synthesis of SG, the nitric acid was added into precursor solution to control the pH = 2

Table 2
The summary of characterizations by different measurements of P25, SG, FT1, FT1.5, FT2 photocatalysts.

Entry	Item	P25	SG	FT1	FT1.5	FT2
1	Particle size (from DLS) (nm)	–	181.5	214.3	155.8	535.4
2	Particle size[a] (from TEM) (nm)	–	13.1	44.5	44	79.6
3	Crystalline size (from XRD) (nm)	10.9	16.5	10.2	9.8	10.6
4	Band gap[b] (eV)	3.22	3.00	3.23	3.24	3.24
5	BET surface area ($m^2\ g^{-1}$)	50.0	23.9	95.6	102.2	47.1
6	$Ti^{3+}/(Ti^{3+}+Ti^{4+})$ (from XPS) (%)	–	3.7	18	20.2	20.8

– No information.
[a] An edge length for FT1, FT1.5 and FT2 photocatalysts.
[b] K-M function was applied.

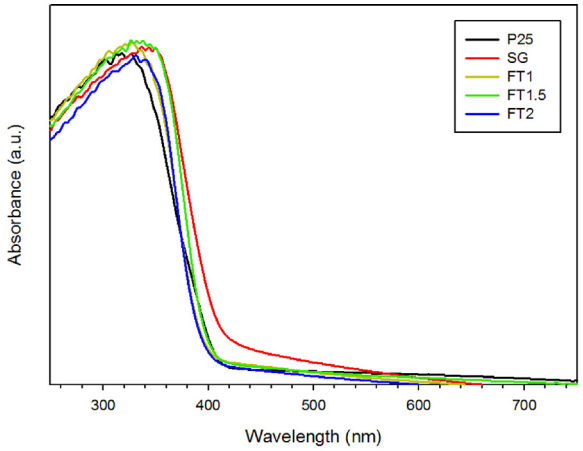

Fig. 2. The diffuse reflectance UV–vis spectra of P25, SG, FT1, FT1.5, FT2 photocatalysts.

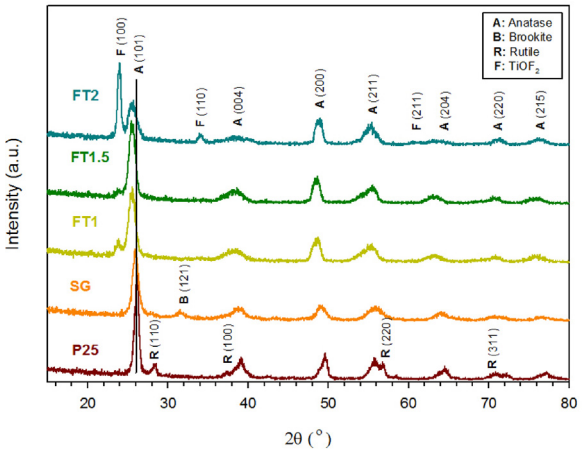

Fig. 3. The powder X-ray diffraction patterns of P25, SG, FT1, FT1.5, FT2 photocatalysts.

where was at the isoelectric point of TiO_2 sol-gel. Previous study also proved that nitric acid can act as a nitrogen source to synthesize N-doped TiO_2 by sol-gel method [34]. However, the color change has not been observed when fluorine atoms are doped into TiO_2 lattice [32,35]. This is why only SG showed yellowish color. The spectra would be further expressed by the Kubelka-Munk (K-M or F(R)) method to calculate the band gap of each sample, as shown in Fig. S1 [36]. All values of the derived band gaps are summarized in Table 2.

Fig. 3 shows the XRD patterns of five photocatalysts with their corresponding phases. P25 exhibited the typical anatase (JCPDS no. 21-1272) and rutile (JCPDS no. 21-1276) peaks, while SG displayed mostly anatase peaks with a subtle brookite (JCPDS no. 29-1360) peak at $2\theta = 31.56^\circ$. Note that the brookite phase has usually been found in TiO_2 synthesized by the sol-gel method [37]. For all titania nanosheets (FT1, FT1.5, and FT2), they showed the characteristic anatase peaks at the corresponding positions, $2\theta = 25.5^\circ$, 38.7°, 48.7°, 55.5°, 63.5°, 70.5°, and 76.1°. Among three titania nanosheets, the differences of their 2θ values for each peak were less than 0.1°. However, characteristic titanium oxydifluoride ($TiOF_2$, JCPDS no. 08-0060) peaks were shown simultaneously in these titania nanosheets. FT2 showed three peaks which can be ascribed to $TiOF_2$ at $2\theta = 23.94^\circ$, 34.18° and 60.38°. As for FT1, two peaks could be found at $2\theta = 23.86^\circ$ and 34.24°. Lastly, the FT1.5 only exhibited an extremely small peak at $2\theta = 23.86^\circ$. Since all of the samples were prepared and tested under the same conditions in XRD analysis, it could be determined that the percentage of $TiOF_2$ among these three titania nanosheets were in the following order arrangement: FT2 > FT1 > FT1.5. Moreover, the anatase (001) peaks of P25 and SG were shown at $2\theta = 26.16^\circ$ and 26.00°, while the anatase (001) peaks of FT1, FT1.5, and FT2 were shown at $2\theta = 25.58^\circ$, 25.46°, and 25.52°, respectively. It should be noted that the peaks of dominant anatase (101) peak for these titania nanosheets had a negative shift about 0.5° in comparison with the same anatase (101) peak of P25 and SG. According to the Bragg's Law, the d-spacing (d) and diffraction angle (2θ) are in inverse proportion. Therefore, these negative shifts of anatase (101) peak could be referred to as the broadening of d-spacing, revealing the doping effect of F atoms.

The SEM images as shown in Fig. 4 were used to get the morphology of photocatalysts. SG exhibited the typical granulated particles and FT1, FT1.5, and FT2 all looked like stacked sheets. Furthermore, TF1 and TF1.5 were similar to each other in their sizes while TF2 was evidently larger than TF1 and TF1.5. The particle sizes were further estimated by dynamic light scattering (DLS) and TEM images as summarized in Table 2. The trend of both measurements was the same for titania nanosheets that FT2 > FT1 > FT1.5 in sizes. All values got from DLS measurement were larger than those from direct TEM observations because DLS cannot distinguish the aggregated particles from each other, leading the overestimation of particle sizes. The trend of particle sizes could also be justified by the BET surface area analysis as shown in Table 2. For FT1 and FT1.5, the BET surface areas were 95.6 and 102.2 $m^2\ g^{-1}$ which were quite identical to each other. Nonetheless, FT2 was only half as large as those two for the value of 47.1 $m^2\ g^{-1}$. These values were quite rational according to the SEM observation that FT2 was obviously larger than the other titania nanosheets. The low BET surface area of FT2 might be explained by its crystalline phases which contain a higher percentage of $TiOF_2$ crystalline phase.

High-resolution TEM can acquire more information about morphology as shown in Fig. 5. Fig. 5(a) shows the side view of titania nanosheets and the inset figure clearly displays the d-spacing of (004) anatase crystalline phase was 0.235 nm which is consistent with the theoretical value. Likewise, Fig. 5(b) shows the top view of titania nanosheets and the inset figure demonstrated the d-spacing was 0.19 nm which corresponds to (200) anatase crystalline phase. The above TEM results confirmed the FT1.5 was the

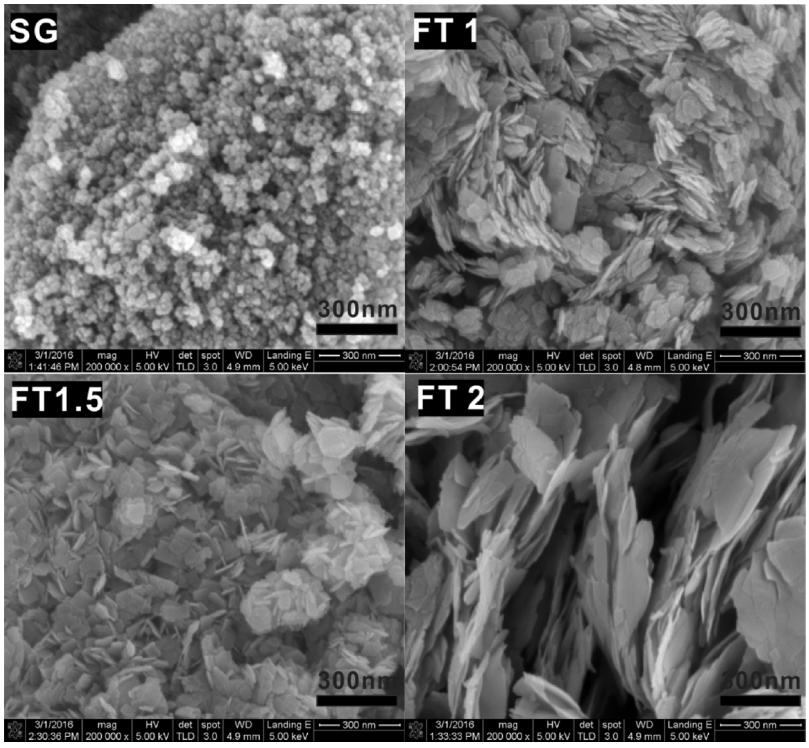

Fig. 4. The SEM images of SG, FT1, FT1.5 and FT2 photocatalysts.

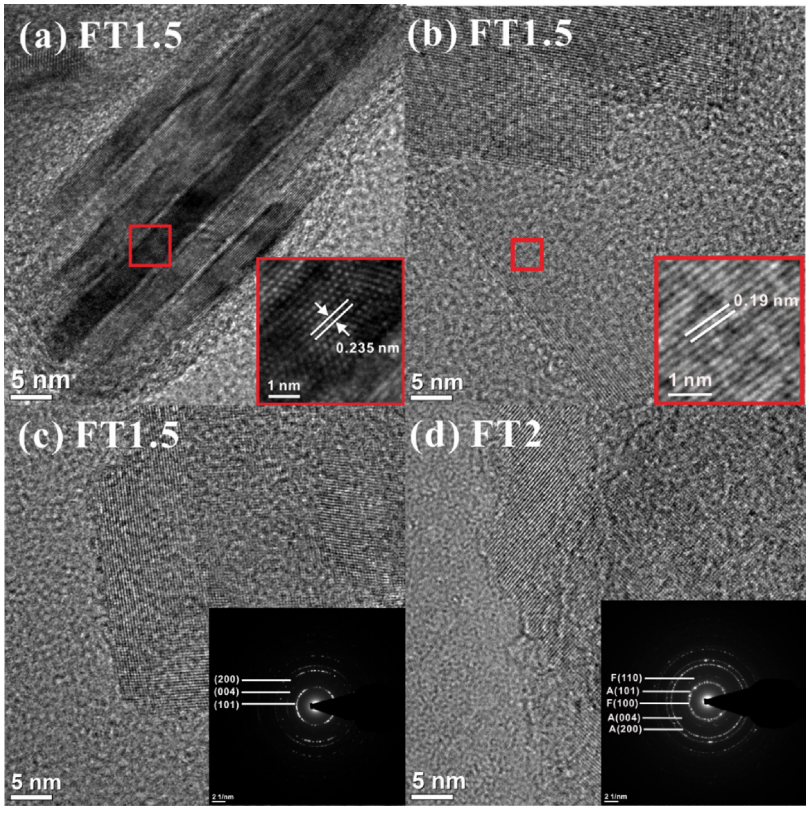

Fig. 5. TEM images for (a) Side view of FT1.5; (b) Top view of FT1.5; (c) SAED pattern of the selected area for FT1.5; (d) SAED pattern of the selected area for FT2.

ultra-thin nanosheets with highly exposed facets along (001) direction. According to the TEM plots, the particle size and thickness for FT1.5 were counted, equaling to 44.04 and 3.60 nm, respectively. The calculated percentage of exposed (001) facet = 73.6% [38]. Moreover, Fig. 5(c) shows the SAED pattern, and note that the universally recognized resolution of spot size is 100 nm so all of the nanosheets which dispersed randomly should be included in this figure. Consequently, SAED exhibited a ring pattern rather

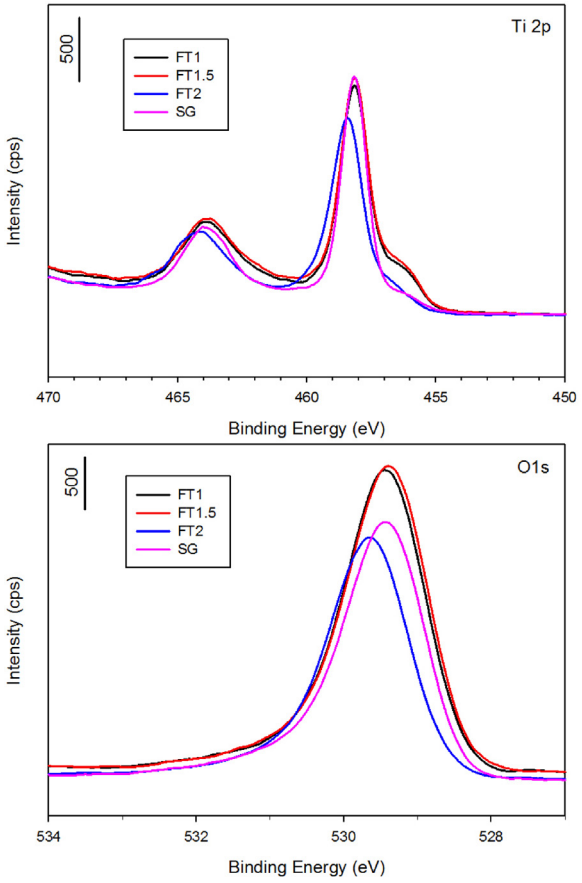

Fig. 6. XPS spectra of Ti 2p and O 1s for FT1, FT1.5, FT2, and SG photocatalysts.

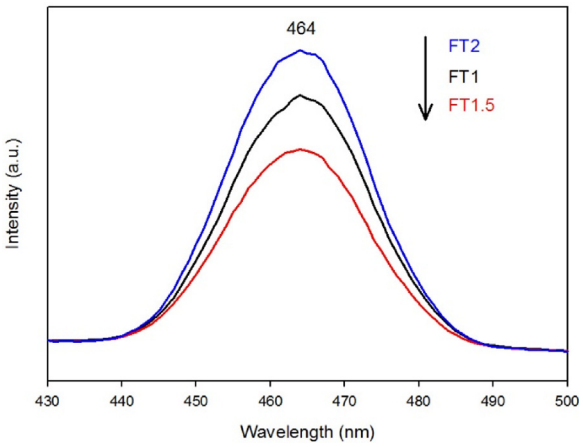

Fig. 7. PL spectra of titania nanosheets.

than a single crystal pattern. Again, the characteristic phases for FT1.5 photocatalysts belonged to anatase phase. For Fig. 5(d), FT2 demonstrated both anatase and $TiOF_2$ ring pattern. Both of the observations from FT1.5 and FT2 were consistent with the XRD pattern.

XPS was used to confirm the chemical states of the elements as shown in Fig. 6. In Ti2p region, the $Ti2p_{3/2}$ main peak positions of FT1, FT1.5, FT2, and SG appeared at 458.15, 458.15, 458.45, and 458.15 eV, respectively. The slightly positive shift of Ti for FT2 in comparison with other samples might due to its higher amount of $TiOF_2$. The F atoms, whose electron negativity is higher than O atoms, can attract more electrons from Ti atoms than O atoms so the Ti atoms in FT2 had this positive shift. Moreover, note that the asymmetric peaks in Ti region were shown for all samples, indicating that not only Ti^{4+} but also Ti^{3+} might exist. The deconvolution results are shown in Fig. S2 and the values of Ti^{3+} percentage for each sample are summarized in Table 2. All titania nanosheets exhibited the values of Ti^{3+} percentage for about 20%, which were much higher than the value of Ti^{3+} percentage for SG photocatalyst of about 4%. This result demonstrated that adding F atoms in precursor solution could raise more Ti^{3+}, whose nature of Ti^{3+} formation has been well explained by using electron paramagnetic resonance (EPR), XPS and the theoretical calculations from density function theory (DFT) [39]. Importantly, it was claimed that Ti^{3+} ions can reduce the recombination rate of electrons and holes generated by light irradiation [37], and then enhance the photocatalytic performance. In O1s region, the main peak positions of FT1, FT1.5, FT2, and SG were emerged at 529.45, 529.40, 529.65 and 529.45, respectively. All positions of peaks in O1s region and in Ti region mentioned above have been proved in many studies [40–42]. Furthermore, the asymmetric peaks in F1s region are also found among FT1, FT1.5, and FT2 titania nanosheets as shown in Fig. S3. The asymmetric peaks could be separated into two peaks at 684.1 and 685.3 eV which corresponds to surface F^- on TiO_2 [37,43,44] and F^- in $TiOF_2$ [45,46], respectively. In this study, TiO_2 nanosheets were synthesized without calcination or base-washing step that both can remove the surface fluorine ions. Lv et al. reported that surface fluorination can greatly enhance the photocatalytic activity of TiO_2 due to the formation of free $^{\bullet}OH$ radicals which are highly reactive [47]. There were no peaks found at 688.3 eV, which is the F^- of F-doped TiO_2 [37]. The same results have been observed by other researchers [37,39] owing to the very low concentration of doped F^- which is below the detection limit in XPS analysis. Thus, we concluded that an F^- ion atom was inserted into TiO_2 to replace an O^{2-} ion, and a Ti^{3+} cation could be generated from Ti^{4+} simultaneously because of the electron compensation.

Photoluminescence spectra was used to verify the recombination rate of electron-hole pairs generated by light irradiation. The PL signals originated from the surface oxygen vacancies and these oxygen vacancies are from the defects of TiO_2 [48]. The oxygen vacancies can contribute the bound exciton luminescence, show the obvious peaks at 464 nm [49]. In the former XPS analysis, the existence of Ti^{3+} among TiO_2 nanosheets has been observed in the deconvolution results for Ti 2p. The Ti^{3+}, which relates to the oxygen vacancy, results from the doped fluorine atoms in TiO_2 lattice. The distortion of the crystal lattice and TiO_2 defect can be also induced by F doping, showing the PL signal. In Fig. 7, the lowest peak of FT1.5 meant it was with the lowest recombination rate of electron-hole pairs and highest separation efficiency. This recombination rate was in the following order arrangement: FT2 > FT1 > FT1.5, which is related to the photo activities of titania nanosheets.

3.2. Elucidating the formation of titania nanosheet

It is worthy to pay attention on the formation of $TiOF_2$ during the synthesize of titania nanosheets. In this study, TBOT and HF were used as the precursor with different ratios. After vigorously mixing, the hydrothermal treatment was conducted in an autoclave at 453 K for 24 h. To understand the transformation mechanism from precursor solution to titania nanosheets, we summarized the literatures using the hydrothermal method with precursor TBOT (97–98%) and HF (40–48%) in different F/Ti ratios to synthesize titania nanosheets at different temperatures and durations in Table 3. The presence of $TiOF_2$ was judged by the XRD pattern at 23.9°.

For entry 1, all conditions except the duration of hydrothermal process kept the same, and it could be found that the $TiOF_2$ did not show in the half-hour hydrothermal process (entry 1-1). When the duration increased, the peak of $TiOF_2$ started to emerge (entry

Table 3
Summary of recent literatures using the hydrothermal method with precursor TBOT and HF at different conditions to synthesize titania nanosheets.

Entry	Synthetic Conditions				Results				Ref.
	F/T atomic ratio	Temp. (K)	Duration (h)	Calcination	[a]Presence of $TiOF_2$	Edge Length (nm)	Thickness (nm)	Exposed (001) facets (%)	
1–1	0.67	433	0.5	No	w/o	–	–	–	[50]
1–2	0.67	433	2.3	No	Presence	–	–	–	
1–3	0.67	433	6	No	Trace	–	–	–	
1–4	0.67	433	24	No	w/o	11	1.6	77	
1–5	1	433	24	No	w/o	25	2.7	82	
2–1	0.8	453	24	No	Presence	19	10	38	[51]
2–2	1.6	453	24	No	Trace	21	4	68	
2–3	2.4	453	24	No	Presence	28	3	80	
3	1	453	24	No	Presence	20–100	20	62	[52]
4	1	453	24	No	Trace	50–80	6	75	[20]
5	1	453	24	No	Trace	–	–	–	[53]
6	1	453	24	No	w/o	70–80	8	75	[54]
7	1	453	24	No	w/o	50–60	10–15	62–71	[44]
8	1	453	36	No	w/o	20–70	4–8	–	[55]
9–1	0	453	24	823 K, 1 h	w/o	–	–	11	[2]
9–2	1	453	24	823 K, 1 h	w/o	–	–	49	
9–3	1.5	453	24	823 K, 1 h	w/o	–	–	58	
9–4	2	453	24	823 K, 1 h	w/o	–	–	72	
9–5	3	453	24	823 K, 1 h	w/o	–	–	83	
10–1	0.67	453	24	No	–	30	7	68	[18]
10–2	1	453	24	No	w/o	40	6	77	
10–3	1.33	453	24	No	–	50	6	80	
10–4	0.67	473	24	No	–	52	8	76	
10–5	1	473	24	No	–	60	7	81	
10–6	1.33	473	24	No	–	130	8	89	

[–] No information.
[a] Judged by XRD pattern at main $TiOF_2$ (100) peak at 23.9° (Presence: can be clear detected without magnification of on-line printed paper; Trace: can be clear detected with magnification of on-line printed paper; w/o: cannot be detected).

1–2, 1–3) and then disappeared finally (entry 1–4). Therefore, it could be concluded that the $TiOF_2$ is the intermediate during the transformation of Ti^{4+} to titania nanosheets (TiO_2), and the duration of the hydrothermal process is one of the key factors to successfully synthesize the pure TiO_2 titania nanosheets. On the other hand, the F/Ti atomic ratio of the precursor, where F^- was from HF and Ti^{4+} was from TBOT, also played a significant role during the synthesis according to the results of entry 2. Overly low F/Ti ratio (F/Ti = 0.8, entry 2-1) or overly high F/Ti ratio (2.4, entry 2–3) was not favorable to eliminate the presence of $TiOF_2$. There existed the optimal F/Ti ratio to get rid of $TiOF_2$ (F/Ti = 1.6, entry 2.2).

In this study, our result was similar to theirs that FT1.5 (F/Ti = 1.5) could suppress the existence of $TiOF_2$, however, a higher amount of $TiOF_2$ was shown in FT2 in comparison with the fluorine-rich sample in the literature (entry 2–3). In the other literature (entry 3 to entry 10), some exhibited the $TiOF_2$ peak in XRD pattern while some did not, though the synthetic conditions (F/T = 1.0, temperature = 453 K, duration = 24 h) were quite identical. A possible reason is the ambiguous definition of duration (that is, experiment described hydrothermal treatment for "X hour" but did not mention whether "X hour" includes the temperature-elevating process or not) and the instrumental difference of the controlled temperature. Since the peak of $TiOF_2$ in most of the papers was not very high so even the slight difference could contribute the presence or not the presence of the $TiOF_2$. On the other hand, it should be noted that there were no $TiOF_2$ peaks of the samples with calcination process (entry 9), so it could be inferred that calcination can transform $TiOF_2$ to titania nanosheet (TiO_2) completely. This observation was proved in Fig. S4 that the $TiOF_2$ could be transformed to anatase TiO_2 after the calcination process at 823 K for 1 h. It is also reported that using TiO_2 nanosheet to conduct the calcination can delay and suppress the phase change from anatase to rutile at higher temperature [47] since the transformation happens at 873 K typically 56].

In summary, the chemical reactions of titania nanosheet formation can be proposed. The first step is the hydrolysis reaction of TBOT, forming $Ti(OH)_4$ as shown in Eq. (4) [57–59]. Secondly, in Eq. (5), $Ti(OH)_4$ can react with HF to produce intermediate $TiOF_2$ through water condensation [57,59]. Lastly, the intermediate $TiOF_2$ can be hydrolyzed again with saturated steam at about 453 K [60], and pH = 2 [61] as shown in Eq. (6). Note that the stoichiometric coefficients of both water and hydrofluoric acid through Eqs. (4)–(6) sum up to zero. That is, both H_2O and HF could be consumed and produced recurrently.

$$Ti(OC_4H_9)_4 + H_2O \rightarrow Ti(OH)_4 + 4(C_4H_9OH)(\text{hydrolysis}) \quad (4)$$

$$Ti(OH)_4 + 2HF \rightarrow TiOF_2 + 3H_2O(\text{watercondensation}) \quad (5)$$

$$TiOF_2 + 2H_2O \rightarrow TiO_2 + 2HF(\text{hydrolysis}) \quad (6)$$

3.3. Photo-SCR for NOx removal

The NO conversions at different temperatures are shown in Fig. 8 to check the activities of photocatalysts. The FT1.5 exhibited the highest NO conversion at every temperature. Additionally, most of the titania nanosheets were more active than P25 and SG at different temperatures expect only one point at 433 K that NO conversion of FT1 and FT2 was less than SG. This phenomenon could be owing to the stability difference of photocatalysts. As shown in Fig. S5, it can be found that the NO conversion was decreasing (i.e. NO concentration was increasing) quickly with reaction time at 433 K for titania nanosheets, while NO conversion was decreasing slightly for P25 and SG. In other words, the photocatalysts for photo-SCR at 433 K were not as stable as the photocatalysts at other lower temperatures (313, 353 and 393 K). As mentioned before, the NO conversion values were calculated based on the last 5 min before the light was turned off, so the instability of photocatalysts led to the lower NO conversion of titania nanosheets. The possible reason is that since the activity of titania nanosheets was better than P25 and SG due to its higher exposed (001) facets, the formation rate of nitrate NO_3^- for titania nanosheets at 433 K was also faster than the rates of P25 and SG. The NO_3^- may block the active sites of photocatalysts resulting in photocatalyst deactivation. Furthermore,

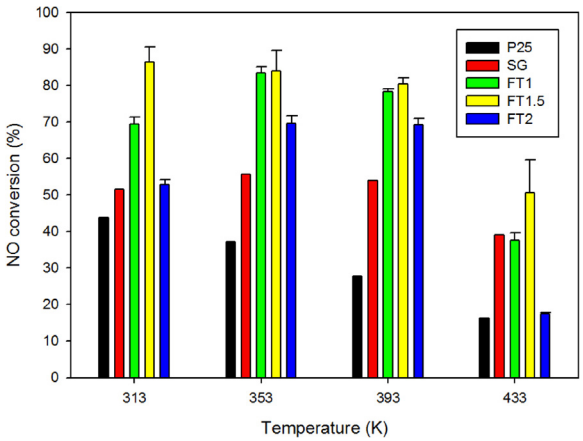

Fig. 8. NO conversion of P25, SG, FT1, FT1.5, and FT2 photocatalysts at different temperatures for photo-SCR reaction (Feed gas compositions: 400 ppmv NO, 2000 ppmv C_4H_{10}, 4 v% H_2O, 4 v% O_2, and N_2 balance.).

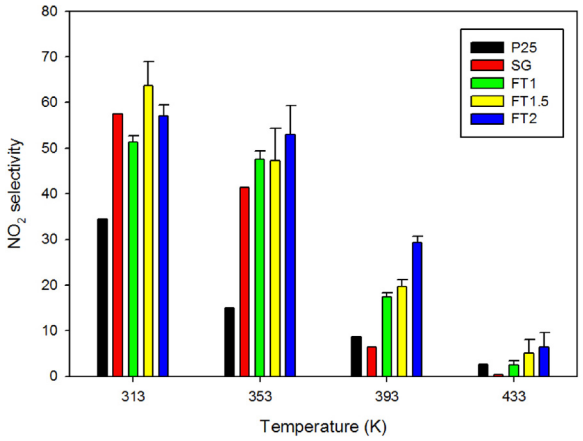

Fig. 9. NO_2 selectivity of P25, SG, FT1, FT1.5, and FT2 photocatalysts at different temperatures for photo-SCR reaction (Feed gas compositions: 400 ppmv NO, 2000 ppmv C_4H_{10}, 4 v% H_2O, 4 v% O_2, and N_2 balance.).

according to the XPS analysis, there existed surface fluorine ions on the surface of titania nanosheets, but not on the surface of P25 and SG. As mentioned, surface fluorination can generate free •OH radicals that promote the oxidation reaction. This can also explain why more NO_3^-, which were from oxidization of NO, were generated on titania nanosheets. Therefore, the control of reaction temperature should be appropriate to prevent the formation of NO_3^-.

The outstanding activity of titania nanosheets, especially for FT1 and FT1.5 could be attributed to the following reasons: high exposed (001) facets, and high BET surface area. In view of the SG and all titania nanosheets, higher exposed (001) facets and higher BET surface of titania nanosheets corresponded to the higher NO conversion. Moreover, among FT1, FT1.5, and FT2, the activity arrangement order was totally consistent with the BET surface area order: FT1.5 > FT1 > FT2. Furthermore, the recombination rates of electron-hole pairs got from PL spectra showed the same trend with the photo-activities. To be more specific, the lower the recombination rate was, the higher the photoactivity would be. On the other hand, considering the main differences between P25 and SG photocatalysts were the BET surface area and the crystalline phases. The rutile phase was not efficient for NO conversion because the BET surface area of P25 was higher than that of SG but NO conversion of P25 was lower than that of SG.

Since the $TiOF_2$ phase presences in the titania nanosheets, it is necessary to know its properties and photoactivity. Lv et al. reported that, even the BET surface area was 23.1 $m^2 g^{-1}$, $TiOF_2$ photoactivity was quite low which was nearly 150 times lower than P25 in X3B dye degradation experiment [62]. Moreover, previous research demonstrated that the photoactivity of TiO_2 nanosheet combined with slightly $TiOF_2$ phase was higher than the pure TiO_2 nanosheet in MB degradation and H_2 production experiments [63]. It can be explained by the better charge separation capability of $TiOF_2$-TiO_2 mixed phase that reduces the recombination rate of electron-hole pairs. However, high amount of $TiOF_2$ phase in the TiO_2 nanosheet would decrease the photoactivity due to the poor photoactivity of $TiOF_2$. Our result was well consistent with those previous researches that FT1.5 with a slightly $TiOF_2$ phase exhibited high photoactivity while FT2 with lots of $TiOF_2$ phases exhibited relative low photoactivity.

The selectivity of NO_2 is shown in Fig. 9. NO_2 is one of the toxic by-products of the photo-SCR reaction. Based on the result, it was obvious that increasing temperature was an important factor to decrease the NO_2 selectivity. Also, we found that NO_2 could be reduced to its minimum value at 433 K for all kinds of photocatalysts. The reaction pathway was proposed in the previous study

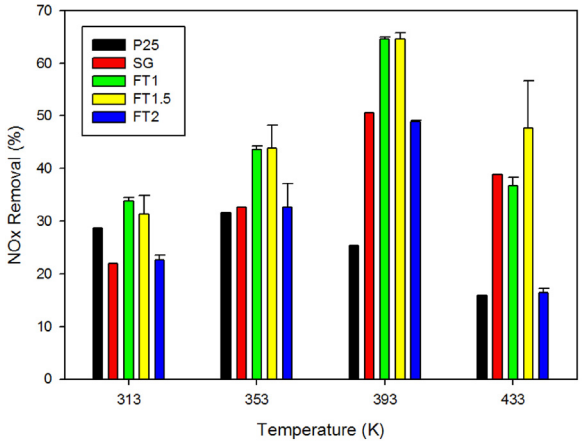

Fig. 10. NOx removal of P25, SG, FT1, FT1.5, and FT2 photocatalysts at different temperatures for photo-SCR reaction (Feed gas compositions: 400 ppmv NO, 2000 ppmv C_4H_{10}, 4 v% H_2O, 4 v% O_2, and N_2 balance.).

that the NO would firstly form NO_2 and then NO_2 further reduced to N_2 with the help of reducing agent at high temperature [24]. Note that the NO_2 selectivity for SG and P25 at every temperature was lower than for titania nanosheets. This can be clarified by the nature of the morphology of catalysts. The holes would easily accumulate on (001) facets while electrons would stay on (101) facets [2]. This might explain why the NO_2 selectivity of titania nanosheets was higher than SG and P25. The more (001) facets exposed, the higher oxidation rate achieved. Moreover, among titania nanosheets, FT2 exhibited the highest NO_2 selectivity while FT1 exhibited the lowest NO_2 selectivity at every temperature except only one inconsistent data point (FT1.5 at 313 K). Again, it could also be interpreted by its percentage of (001) exposed area. In the synthesis of titania nanosheets, it is well-known that higher F/Ti ratio in precursor leads to higher percentage of (001) exposed area [2,18,50,51]. This is why FT2 with largest exposed (001) facets would have the highest NO_2 selectivity.

With regards to environmental points of view, NO conversion and NO_2 selectivity should be considered together, therefore, NOx removal is shown in Fig. 10. At 313 K, the values of NOx removal were low for all photocatalysts due to different reasons. For P25 and SG, it was owing to the relatively low NO conversion as compared to titania nanosheets. For titania nanosheets, it was because of their high NO_2 selectivity. Nonetheless, the NOx removal could be improved by increasing the reaction temperature. Note that it

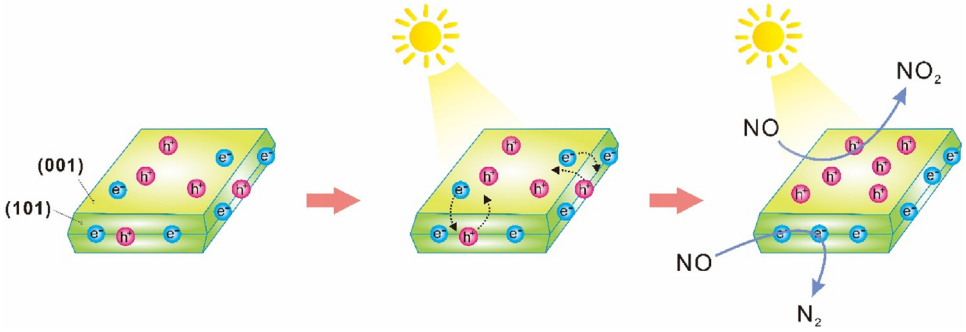

Fig. 11. The role of reactive facets on photo-SCR over titania nanosheet photocatalysts.

was a trade-off relationship between NO conversion and NO_2 selectivity. Increasing the reaction temperature could reduce the NO_2 selectivity but also decrease the NO conversion. For FT1.5 and FT1, the NOx removal reached to their maximum at 393 K so it could be concluded that moderately high temperature was benefited for NOx removal in photo-SCR. For the practical applications, photo-SCR can be used in the post-treatment of exhaust gas or flue gas, which is emitted at high temperature. The waste heat from exhaust gas flue gas can heat up the photocatalyst to not only get the better performance but also prevent water condensation in the pipeline. Overall, it is wholly reasonable to apply at this temperature, 393 K.

3.4. Particular role of reactive facets on photo-SCR for NOx removal

In conclusion, FT1.5 had the superior photoactivity according to the results of NO conversion for different photocatalysts. However, if taking the formation of NO_2 into account to check the NOx removals for all photocatalysts, both FT1 and FT1.5 exhibited good performance. The simplified mechanism was proposed to explain the role of (001) and (101) facets of titania nanosheets as depicted in Fig. 11. Oxidation reaction occurred on the (001) facets and reduction reaction occurred on the (101) facets. FT1.5 with higher percentage of exposed (001) facets produced more NO_2 than FT1 with lower percentage of exposed (001) facets. This might explain that why FT1 and FT1.5 had the close performance of NOx removal even though the photoactivity of FT1.5 was better than FT1. Therefore, it is suggested that titania nanosheets were not only had good performance in photocatalytic water splitting [20], dye degradation and CO_2 reduction [22], but also in NOx abatement. Moreover, FT1.5 seems to be a highly efficient photocatalyst not only in this study, but also in other literature with the similar F/Ti ratio (closed to 1.5), but different applications which include CO_2 reduction and MB degradation [2,51]. Thus, we strongly recommended following this synthetic process to get the extraordinary titania nanosheet.

4. Conclusions

In this study, titania nanosheet photocatalysts are successfully synthesized by hydrothermal method. The pathway of transformation from TBOT to TiO_2 nanosheet is clearly revealed and shown that $TiOF_2$ is the intermediate during the synthesis process. One of the best synthetic processes for TiO_2 nanosheet is to use TBOT and HF with the F/Ti atomic ratio = 1.5 at 453 K for 24 h in hydrothermal treatment. The titania nanosheet synthesized under this condition can get rid of the formation $TiOF_2$. It is worth mentioning that the synthesized TiO_2 nanosheet exhibits outstanding performance in photocatalysis due to its high BET surface area and highly exposed (001) facet in comparison with the TiO_2 synthesized by sol-gel method and P25. The NO conversion of titania nanosheets is found to have a better NO conversion than that of SG and P25, but their NO_2 selectivity is also high because of its highly exposed (001) facets. To the best of our knowledge, this is the first time the particular role of reactive facets on photocatalytic NOx removal has been systematically studied. There was a trade-off relationship to get the best performance of photo-SCR using titania nanosheets. Our study also reveals that FT1.5 displayed the highly efficient NOx removal at 393 K.

Acknowledgements

The research was investigated under the bilateral Taiwanese-Polish Joint Research Project. The authors gratefully acknowledge the Ministry of Science and Technology, Taiwan, for financial support under grant NSC 103-2923-E-002-002-MY3, as well as National Centre for Research and Development, Poland, agreement No. DKO/PL-TW1/2/2013.

Appendix A. Supplementary data

Supplementary data associated with this article can be found, in the online version, at http://dx.doi.org/10.1016/j.apcatb.2017.07.077.

References

[1] M. Kampa, E. Castanas, Human health effects of air pollution, Environ. Pollut. 151 (2008) 362–367.
[2] J. Yu, J. Low, W. Xiao, P. Zhou, M. Jaroniec, Enhanced photocatalytic CO2-reduction activity of anatase TiO2 by coexposed {001} and {101} facets, J. Am. Chem. Soc. 136 (2014) 8839–8842.
[3] W.S. Tunnicliffe, P.S. Burge, J.G. Ayres, Effect of domestic concentrations of nitrogen dioxide on airway responses to inhaled allergen in asthmatic patients, Lancet 344 (1994) 1733–1736.
[4] A.H. Wolfe, J.A. Patz, Reactive nitrogen and human health: acute and long-term implications, Ambio 31 (2002) 120–125.
[5] W.L. Chameides, F. Fehsenfeld, M.O. Rodgers, C. Cardelino, J. Martinez, D. Parrish, W. Lonneman, D.R. Lawson, R.A. Rasmussen, P. Zimmerman, J. Greenberg, P. Mlddleton, T. Wang, Ozone precursor relationships in the ambient atmosphere, J. Geophys. Res. 97 (1992) 6037–6055.
[6] R.M. Harrison, A.R. Deacon, M.R. Jones, R.S. Appleby, Sources and processes affecting concentrations of PM10 and PM2.5 particulate matter in Birmingham (U.K.), Atmos. Environ. 31 (1997) 4103–4117.
[7] M. Lippmann, Health effects of ozone: a critical review, JAPCA 39 (1989) 672–695.
[8] N. Li, M. Hao, R.F. Phalen, W.C. Hinds, A.E. Nel, Particulate air pollutants and asthma: a paradigm for the role of oxidative stress in PM-induced adverse health effects, J. Clin. Immunol. 109 (2003) 250–265.
[9] J. Lasek, Y.-H. Yu, J.C.S. Wu, Removal of NOx by photocatalytic processes, J. Photochem. Photobiol. C 14 (2013) 29–52.
[10] B. Ramachandran, R.G. Herman, S. Choi, H.G. Stenger, C.E. Lyman, J.W. Sale, Testing zeolite SCR catalysts under protocol conditions for NOx abatement from stationary emission sources, Catal. Today 55 (2000) 281–290.
[11] K. Teramura, T. Tanaka, S. Yamazoe, K. Arakaki, T. Funabiki, Kinetic study of photo-SCR with NH3 over TiO2, Appl. Catal. B 53 (2004) 29–36.
[12] I.H. Su, J.C.S. Wu, Photo selective catalytic reduction of nitric oxide with propane at room temperature, Catal. Commun. 10 (2009) 1534–1537.
[13] A.A. Lisachenko, R.V. Mikhailov, L.L. Basov, B.N. Shelimov, M. Che, Photocatalytic reduction of NO by CO on titanium dioxide under visible light irradiation, J. Phys. Chem. C 111 (2007) 14440–14447.

[14] E. Stamper, R.L. Koral, Handbook of Air Conditioning, Heating, and Ventilating, 3 ed., Industrial Press Inc., New York, 1979.
[15] H.G. Yang, C.H. Sun, S.Z. Qiao, J. Zou, G. Liu, S.C. Smith, H.M. Cheng, G.Q. Lu, Anatase TiO2 single crystals with a large percentage of reactive facets, Nature 453 (2008) 638–641.
[16] M. Lazzeri, A. Vittadini, A. Selloni, Structure and energetics of stoichiometric TiO2 anatase surfaces, Phys. Rev. B 63 (2001) 155409.
[17] U. Diebold, The surface science of titanium dioxide, Surf. Sci. Rep. 48 (2003) 53–229.
[18] X. Han, Q. Kuang, M. Jin, Z. Xie, L. Zheng, Synthesis of titania nanosheets with a high percentage of exposed (001) facets and related photocatalytic properties, J. Am. Chem. Soc. 131 (2009) 3152–3153.
[19] Q. Xiang, K. Lv, J. Yu, Pivotal role of fluorine in enhanced photocatalytic activity of anatase TiO2 nanosheets with dominant (0 0 1) facets for the photocatalytic degradation of acetone in air, Appl. Catal. B 96 (2010) 557–564.
[20] J. Yu, L. Qi, M. Jaroniec, Hydrogen production by photocatalytic water splitting over Pt/TiO2 nanosheets with exposed (001) facets, J. Phys. Chem. C 114 (2010) 13118–13125.
[21] Q. Xiang, J. Yu, M. Jaroniec, Enhanced photocatalytic H2-production activity of graphene-modified titania nanosheets, Nanoscale 3 (2011) 3670–3678.
[22] H. Xu, S. Ouyang, P. Li, T. Kako, J. Ye, High-active anatase TiO2 nanosheets exposed with 95% {100} facets toward efficient H2 evolution and CO2 photoreduction, ACS Appl. Mater. Interfaces 5 (2013) 1348–1354.
[23] C.P. Sajan, S. Wageh, A.A. Al-Ghamdi, J. Yu, S. Cao, TiO2 nanosheets with exposed {001} facets for photocatalytic applications, Nano Res. 9 (2016) 3–27.
[24] J.C.-C. Yu, V.-H. Nguyen, J. Lasek, D.X. Li, J.C.S. Wu, Competitive reaction pathway for photo and thermal catalytic removal of NO with hydrocarbon in flue gas under elevated temperatures, Catal. Commun. 84 (2016) 40–43.
[25] Z. Zheng, B. Huang, X. Qin, X. Zhang, Y. Dai, M. Jiang, P. Wang, M.-H. Whangbo, Highly efficient photocatalyst: TiO2 microspheres produced from TiO2 nanosheets with a high percentage of reactive {001} facets, Chem. Eur. J. 15 (2009) 12576–12579.
[26] A. Monshi, M.R. Foroughi, M.R. Monshi, Modified scherrer equation to estimate more accurately nano-crystallite size using XRD, World J. Nano Sci. Eng. 2 (2012) 154–160.
[27] M.C. Biesinger, L.W.M. Lau, A.R. Gerson, R.S.C. Smart, Resolving surface chemical states in XPS analysis of first row transition metals, oxides and hydroxides: Sc, Ti, V, Cu and Zn, Appl. Surf. Sci. 257 (2010) 887–898.
[28] J.C.C. Yu, V.-H. Nguyen, J. Lasek, S.-W. Chiang, D.X. Li, J.C.S. Wu, NOx abatement from stationary emission sources by photo-assisted SCR: lab-scale to pilot-scale studies, Appl. Catal. A 523 (2016) 294–303.
[29] J. Li, H. Chang, L. Ma, J. Hao, R.T. Yang, Low-temperature selective catalytic reduction of NOx with NH3 over metal oxide and zeolite catalysts—a review, Catal. Today 175 (2011) 147–156.
[30] N. Bowering, G.S. Walker, P.G. Harrison, Photocatalytic decomposition and reduction reactions of nitric oxide over Degussa P25, Appl. Catal. B 62 (2006) 208–216.
[31] R. Asahi, T. Morikawa, T. Ohwaki, K. Aoki, Y. Taga, Visible-light photocatalysis in nitrogen-doped titanium oxides, Science 293 (2001) 269.
[32] D. Li, N. Ohashi, S. Hishita, T. Kolodiazhnyi, H. Haneda, Origin of visible-light-driven photocatalysis: a comparative study on N/F-doped and N–F-codoped TiO2 powders by means of experimental characterizations and theoretical calculations, J. Solid State Chem. 178 (2005) 3293–3302.
[33] T. Sano, N. Negishi, K. Koike, K. Takeuchi, S. Matsuzawa, Preparation of a visible light-responsive photocatalyst from a complex of Ti4+ with a nitrogen-containing ligand, J. Mater. Chem. 14 (2004) 380–384.
[34] X. Cheng, X. Yu, Z. Xing, L. Yang, Synthesis and characterization of N-doped TiO2 and its enhanced visible-light photocatalytic activity, Arab. J. Chem. 9 (2016) S1706–S1711.
[35] A. Stashans, S. Lunell, R.W. Grimes, Theoretical study of perfect and defective TiO2 crystals, J. Phys. Chem. Solids 57 (1996) 1293–1301.
[36] P. Kubelka, New contributions to the optics of intensely light-scattering materials. Part I, J. Opt. Soc. Am. 38 (1948) 448–457.
[37] J.C. Yu, Ho Yu, Zhang Jiang, Effects of F- doping on the photocatalytic activity and microstructures of nanocrystalline TiO2 powders, Chem. Mater. 14 (2002) 3808–3816.
[38] J.-D. Peng, H.-H. Lin, C.-T. Lee, C.-M. Tseng, V. Suryanarayanan, R. Vittal, K.-C. Ho, Hierarchically assembled microspheres consisting of nanosheets of highly exposed (001)-facets TiO2 for dye-sensitized solar cells, RSC Adv. 6 (2016) 14178–14191.
[39] A.M. Czoska, S. Livraghi, M. Chiesa, E. Giamello, S. Agnoli, G. Granozzi, E. Finazzi, C.D. Valentin, G. Pacchioni, The nature of defects in fluorine-doped TiO2, J. Phys. Chem. C 112 (2008) 8951–8956.
[40] X. Chen, L. Liu, P.Y. Yu, S.S. Mao, Increasing solar absorption for photocatalysis with black hydrogenated titanium dioxide nanocrystals, Science 331 (2011) 746.
[41] M.S. Lazarus, T.K. Sham, X-ray photoelectron spectroscopy (XPS) studies of hydrogen reduced rutile (TiO2-x) surfaces, Chem. Phys. Lett. 92 (1982) 670–674.
[42] Z. Zheng, B. Huang, J. Lu, Z. Wang, X. Qin, X. Zhang, Y. Dai, M.-H. Whangbo, Hydrogenated titania: synergy of surface modification and morphology improvement for enhanced photocatalytic activity, Chem. Commun. 48 (2012) 5733–5735.
[43] H. Park, W. Choi, Effects of TiO2 surface fluorination on photocatalytic reactions and photoelectrochemical behaviors, J. Phys. Chem. B 108 (2004) 4086–4093.
[44] K. Dai, L. Lu, Q. Liu, G. Zhu, Q. Liu, Z. Liu, Graphene oxide capturing surface-fluorinated TiO2 nanosheets for advanced photocatalysis and the reveal of synergism reinforce mechanism, Dalton Trans. 43 (2014) 2202–2210.
[45] D. Li, H. Haneda, N.K. Labhsetwar, S. Hishita, N. Ohashi, Visible-light-driven photocatalysis on fluorine-doped TiO2 powders by the creation of surface oxygen vacancies, Chem. Phys. Lett. 401 (2005) 579–584.
[46] J. Zhu, F. Lv, S. Xiao, Z. Bian, G. Buntkowsky, C. Nuckolls, H. Li, Covalent attachment and growth of nanocrystalline films of photocatalytic TiOF2, Nanoscale 6 (2014) 14648–14651.
[47] K. Lv, Q. Xiang, J. Yu, Effect of calcination temperature on morphology and photocatalytic activity of anatase TiO2 nanosheets with exposed {001} facets, Appl. Catal. B: Environ. 104 (2011) 275–281.
[48] B. Bharti, S. Kumar, H.-N. Lee, R. Kumar, Formation of oxygen vacancies and Ti3+ state in TiO2 thin film and enhanced optical properties by air plasma treatment, Sci. Rep. 6 (2016) 32355.
[49] C. Wang, H. Shi, Y. Li, Synthesis and characterization of natural zeolite supported Cr-doped TiO2 photocatalysts, Appl. Surf. Sci. 258 (2012) 4328–4333.
[50] X.H. Yang, Z. Li, G. Liu, J. Xing, C. Sun, H.G. Yang, C. Li, Ultra-thin anatase TiO2 nanosheets dominated with {001} facets: thickness-controlled synthesis, growth mechanism and water-splitting properties, CrystEngComm 13 (2011) 1378–1383.
[51] F. Tian, Y. Zhang, J. Zhang, C. Pan, Raman spectroscopy a new approach to measure the percentage of anatase TiO2 exposed (001) facets, J. Phys. Chem. C 116 (2012) 7515–7519.
[53] S. Zhu, S. Liang, Q. Gu, L. Xie, J. Wang, Z. Ding, P. Liu, Effect of Au supported TiO2 with dominant exposed {0 0 1} facets on the visible-light photocatalytic activity, Appl. Catal. B 119–120 (2012) 146–155.
[54] J. Yu, J. Fan, K. Lv, Anatase TiO2 nanosheets with exposed (001) facets: improved photoelectric conversion efficiency in dye-sensitized solar cells, Nanoscale 2 (2010) 2144–2149.
[55] L. Liu, Z. Ji, W. Zou, X. Gu, Y. Deng, F. Gao, C. Tang, L. Dong, In situ loading transition metal oxide clusters on TiO2 nanosheets as co-catalysts for exceptional high photoactivity, ACS Catal. 3 (2013) 2052–2061.
[56] D.A.H. Hanaor, C.C. Sorrell, Review of the anatase to rutile phase transformation, J. Mater. Sci. 46 (2011) 855–874.
[57] S. Mahshid, M. Askari, M.S. Ghamsari, Synthesis of TiO2 nanoparticles by hydrolysis and peptization of titanium isopropoxide solution, J. Mater. Process. Technol. 189 (2007) 296–300.
[58] S. Qourzal, A. Assabbane, Y. Ait-Ichou, Synthesis of TiO2 via hydrolysis of titanium tetraisopropoxide and its photocatalytic activity on a suspended mixture with activated carbon in the degradation of 2-naphthol, J. Photochem. Photobiol. A 163 (2004) 317–321.
[59] B.E. Yoldas, Hydrolysis of titanium alkoxide and effects of hydrolytic polycondensation parameters, J. Mater. Sci. 21 (1986) 1087–1092.
[60] J.H. Moss, A. Wright, Titanium(IV) oxydifluoride, J. Fluorine Chem. 5 (1975) 163–167.
[61] Z. Wang, B. Huang, Y. Dai, X. Zhu, Y. Liu, X. Zhang, X. Qin, The roles of growth conditions on the topotactic transformation from TiOF2 nanocubes to 3D hierarchical TiO2 nanoboxes, CrystEngComm 15 (2013) 3436–3441.
[62] K. Lv, J. Yu, L. Cui, S. Chen, M. Li, Preparation of thermally stable anatase TiO2 photocatalyst from TiOF2 precursor and its photocatalytic activity, J. Alloys Compd 509 (2011) 4557–4562.
[63] Y. Zhang, T. Xia, M. Shang, P. Wallenmeyer, D. Katelyn, A. Peterson, J. Murowchick, L. Dong, X. Chen, Structural evolution from TiO2 nanoparticles to nanosheets and their photocatalytic performance in hydrogen generation and environmental pollution removal, RSC Adv. 4 (2014) 16146–16152.